Nanoscale Advances

PAPER

View Article Online
View Journal | View Issue

Cite this: *Nanoscale Adv.*, 2019, **1**, 735

Starting a subnanoscale tank tread: dynamic fluxionality of boron-based $B_{10}Ca$ alloy cluster†

Ying-Jin Wang,‡[ab] Lin-Yan Feng‡[a] and Hua-Jin Zhai *[a]

Alloying an elongated B_{10} cluster with Ca is shown to give rise to a dynamically fluxional $B_{10}Ca$ cluster, the latter behaving like a tank tread at the subnanoscale. Computer global search identifies the $B_{10}Ca$ C_2 (^{1}A) global-minimum structure, which is chiral in nature and retains the quasi-planar moiety of bare B_{10} cluster with Ca capped at one side, forming a half-sandwich. The rotation barrier of $B_{10}Ca$ cluster is reduced with respect to B_{10} by one order of magnitude, down to 1 kcal mol^{-1} at the PBE0/6-311+G* level, which demonstrates structural fluxionality at 600 K and beyond *via* molecular dynamics simulations. Structurewise, the Ca alloying in $B_{10}Ca$ cluster generates rhombic defect holes, preactivating the species and making it flexible against deformation. Chemical bonding analyses indicate that the $B_{10}Ca$ cluster is a charge-transfer $[B_{10}]^{2-}[Ca]^{2+}$ complex, being doubly π/σ aromatic with the 6π and 10σ electron-counting. Such a pattern offers ideal π/σ delocalization and facilitates fluxionality. In contrast, bare B_{10} cluster has conflicting aromaticity with 6π and 8σ electrons, which is nonfluxional with a barrier of 12 kcal mol^{-1}. Double π/σ aromaticity *versus* conflicting aromaticity is a key mechanism that distinguishes between fluxional $B_{10}Ca$ and nonfluxional B_{10} clusters, offering a compelling example that the concept of aromaticity (and double aromaticity) can be exploited to design dynamically fluxional nanosystems.

Received 29th September 2018
Accepted 6th November 2018

DOI: 10.1039/c8na00256h

rsc.li/nanoscale-advances

1. Introduction

Molecular rotors are interesting nanoscale or subnanoscale systems,[1–18] in which the constituent fragments move collectively and concertedly against each other, akin to nanomachines. Such nanosystems are rare in chemistry and were primarily discovered during the past decade. Boron appears to be a magic element for nanorotors. Several types of boron-based nanorotors have been developed. Firstly, a Wankel motor B_{19}^- cluster was described by Merino and coworkers[1] with a negligible in-plane rotation barrier (less than 0.1 kcal mol^{-1}), immediately following an experimental study of the gas-phase B_{19}^- cluster with concentric dual π aromaticity *via* photoelectron spectroscopy (PES) in 2010.[19] Similar molecular dynamics was discussed earlier in mixed B–C clusters (C_2B_8, $C_3B_9^{3+}$, and $C_5B_{11}^+$),[2] although those species are highly energetic on their potential energy surfaces and thus not viable. Molecular Wankel motors have since been expanded to other systems,[3–9] such as the B_{13}^+ cluster. Second, Zhai and coworkers[10] discovered in 2015 the so-called subnanoscale tank treads, which feature elongated rather than circular geometries with a peripheral ring gliding freely around an elongated inner core. Typical examples are the B_{11}^- and B_{11} clusters, which have a rotation barrier of 0.35 and 0.60 kcal mol^{-1}, respectively. An isoelectronic $B_{10}C$ model cluster[12] was designed subsequently for mechanistic insights into subnanoscale tank treads. Third, a binary Mg_2B_8 cluster was shown to function like a nanocompass[14] and a coaxial triple-layered $Be_6B_{11}^-$ cluster was characterized in 2017 with dual dynamic modes: revolution (orbiting) of the peripheral B_{11} ring *versus* rotation (twisting) of the prismatic Be_6 core.[15] Intriguingly, the $Be_6B_{11}^-$ cluster mimics the dynamic Earth-Moon system at the subnanoscale and yet miniaturizes the latter in size by 18 orders of magnitude.

The ultimate mechanisms of boron-based nanorotors should lie in the electron-deficiency of boron, which leads to highly unusual geometries of boron clusters,[19–36] featuring planar or quasi-planar (2D) structures up to 40 atoms for anions.[30] Among other notable boron clusters are a bowl-like B_{36} borophene[29] and cage-like B_{40}^-/B_{40} borospherenes.[30,37] In terms of chemical bonding, boron clusters are governed by π/σ aromaticity, antiaromaticity, double aromaticity, and

[a]*Nanocluster Laboratory, Institute of Molecular Science, Shanxi University, Taiyuan 030006, China. E-mail: hj.zhai@sxu.edu.cn*

[b]*Department of Chemistry, Xinzhou Teachers University, Xinzhou 034000, China*

† Electronic supplementary information (ESI) available: A short movie extracted from the BOMD simulation at 900 K for $B_{10}Ca$ cluster; Cartesian coordinates for GM structures of $B_{10}Ca$ and B_{10} at the PBE0/6-311+G* level (Table S1); alternative optimized structures of $B_{10}Ca$ at PBE0 (Fig. S1); optimized GM and TS structures of B_{10} and $B_{10}Ca$ at PBE0 with bond distances indicated (Fig. S2); natural atomic charges for GM and TS structures of B_{10} and $B_{10}Ca$ (Fig. S3); CMOs of two $B_{10}Ca$ TS structures (Fig. S4 and S5); ELFs and AdNDP data of $B_{10}Ca$ TS_2 structure (Fig. S6); CMOs of B_{10} GM and TS structures (Fig. S7 and S8); and ELFs and AdNDP data of B_{10} TS structure (Fig. S9). See DOI: 10.1039/c8na00256h

‡ These authors contributed equally to this work.

conflicting aromaticity,[35] which underlie their 2D geometries (as well as their unique structural dynamics). Note that the delocalized π/σ electrons in boron clusters are clouded over a 2D plane,[19,25–36] rather than on a single ring such as in benzene.

It is of fundamental importance to "tune" the rotation barrier of molecular rotors, which not only provides key insights into mechanisms for structural dynamics, but also facilitates control of the movements: halting or starting. Merino and coworkers[7] showed that one C substitution stops the B_{19}^- Wankel motor, resulting in a nonfluxional $B_{18}C$ cluster with a barrier of 27.6 kcal mol^{-1}. On the other hand, Popov *et al.*[17] reported that complexation of B_{12} with a metal atom can reduce the rotation barrier of half-sandwich RhB_{12}^- and CoB_{12}^- clusters from 19.5 kcal mol^{-1} down to 8.7–8.9 kcal mol^{-1}. Likewise, Liu *et al.*[18] designed a metal doped IrB_{12}^- Wankel motor with a barrier of 5.0 kcal mol^{-1}. Nevertheless, these barriers are still quite substantial. It is highly desirable to further reduce the barrier, for example, down to 1 kcal mol^{-1} or less.

We shall meet the above challenge using the $B_{10}Ca$ and B_{10} clusters. The clusters are chosen for a couple of reasons. First, the bare B_{10} cluster is known to be nonfluxional, with a *triangularly close-packed* 2D structure. Second, its *elongated shape* intuitively makes it rather challenging to control or reduce the dynamic barrier. Lastly, as will be shown below, the B_{10} cluster is an unusual bonding system with $6\pi/8\sigma$ *conflicting aromaticity*. Thus, the present work offers a case to tune/control dynamic fluxionality using the concepts of aromaticity, double aromaticity, and antiaromaticity. The strategy has not been exploited in the literature, to our knowledge.

In this contribution, we report on the structural, bonding, and dynamic properties of a binary $B_{10}Ca$ cluster using quantum chemical calculations and chemical bonding analyses. The alloy cluster assumes a half-sandwich structure, in which an elongated B_{10} moiety largely inherits that of bare B_{10} cluster (with subtle variations) and the Ca atom is capped on the B_{10} moiety. This alloy cluster is used to tune the dynamics of bare B_{10} cluster, starting structural fluxionality of the $B_{10}Ca$ cluster as a sub-nanoscale tank tread. The rotation barrier is effectively reduced by one order of magnitude and down to 1 kcal mol^{-1} for $B_{10}Ca$ cluster at the PBE0 level, in contrast to 12.32 kcal mol^{-1} for the B_{10} cluster. The relevant mechanisms are fully elucidated *via* chemical bonding analyses, which should guide further designs of fluxional dynamic nanosystems.

2. Methods

Global-minimum (GM) search for the $B_{10}Ca$ cluster was conducted using the unbiased Coalescence Kick (CK) algorithm[38,39] at the B3LYP/3-21G level. About 3000 stationary points were probed on the potential energy surface. Low-lying isomers were then fully reoptimized and their relative energies evaluated at the PBE0/6-311+G* level.[40,41] Vibrational frequencies were calculated at the same level to ensure that the reported structures are true minima unless stated otherwise. To benchmark the energetics, single-point CCSD(T) calculations[42–44] were carried out for the top two lowest-energy structures, that is, at the CCSD(T)/6-311+G*//PBE0/6-311+G* level, which also serve to validate the PBE0 method for the present system. The QST2 and intrinsic reaction coordinate (IRC) calculations were performed at the PBE0/6-311+G* level to locate and confirm transition state (TS) structures associated with in-plane rotation.

Natural bond orbital (NBO)[45] calculations were carried out at the PBE0/6-311G* level to obtain Wiberg bond indices (WBIs) and natural atomic charges. Chemical bonding was understood *via* CMO analyses and AdNDP.[46] The latter was done at the PBE0/6-31G level owing to the fact that such analysis is not sensitive to the level of theory or basis sets used. Born–Oppenheimer molecular dynamics (BOMD) simulations were accomplished at the PBE/DZVP level using the CP2K package.[47] All electronic structure calculations were performed using Gaussian 09.[48] AdNDP analyses were conducted using the AdNDP program.[46] The visualization of AdNDP results was realized using Molekel 5.4.0.8.[49]

3. Results

3.1. Global-minimum and transition-state structures of the $B_{10}Ca$ cluster

The GM structure of $B_{10}Ca$ (C_2, ^1A) cluster at the PBE0/6-311+G* level is shown in Fig. 1, along with that of bare B_{10} (C_{2h}, ^1A_g) cluster. Alternative top 30 low-lying structures of $B_{10}Ca$ cluster, as identified from computer CK search and reoptimized at the PBE0/6-311+G* level, are presented in Fig. S1 (ESI†). The nearest isomeric structure is 0.83 eV higher in energy at PBE0 and 0.85 eV at single-point CCSD(T), suggesting that the $B_{10}Ca$ GM structure is well defined on its potential energy surface. The $B_{10}Ca$ (C_2, ^1A) cluster (Fig. 1b) is chiral in nature. It contains a bowl-like convex B_{10} fragment onto which the Ca atom caps, forming a half-sandwich complex. It is 4.48 Å in length and 3.35 Å in width (with a length-to-width ratio of 1.34), which has an elongated overall shape and yet it is more circular than bare B_{10} cluster.[50] The peripheral B_8 ring is not perfectly planar, and inner B9 and B10 atoms are popped out from the ring by about 0.8 Å.[51] Note that the B_{10} fragment of $B_{10}Ca$ (C_2, ^1A) largely inherits the bare B_{10} cluster in geometry (Fig. 1a), except that the latter has C_{2h} symmetry with sort of a rugged surface (atom B9 being slightly out-of-plane toward inside and B10 toward the opposite side), which is likely due to mismatch in size between the B_2 core and peripheral B_8 ring.

The $B_{10}Ca$ GM cluster has a soft rotation mode (188.0 cm^{-1}). Following the mode one reaches, *via* QST2 and IRC calculations, two TS_1/TS_2 structures (Fig. 1b) with an imaginary frequency of 102.5i and 207.4i cm^{-1}, respectively, were observed. Both TS_1 and TS_2 have C_{2v} symmetry and the former is practically circular.[50] The IRC data confirm that the two TS structures are truly associated with the GM, corresponding to a clockwise/anticlockwise rotation of the peripheral B_8 ring around the B_2 core. Their rotation barriers are 0.95 and 1.25 kcal mol^{-1} at PBE0, respectively. In contrast, the TS structure of bare B_{10} cluster (Fig. 1a) has C_s symmetry. The energy barrier amounts to 12.32 kcal mol^{-1} at PBE0, one order of magnitude greater than those of $B_{10}Ca$ cluster. Notable structural changes occur between GM and TS of the B_{10} cluster: expansion at one end,

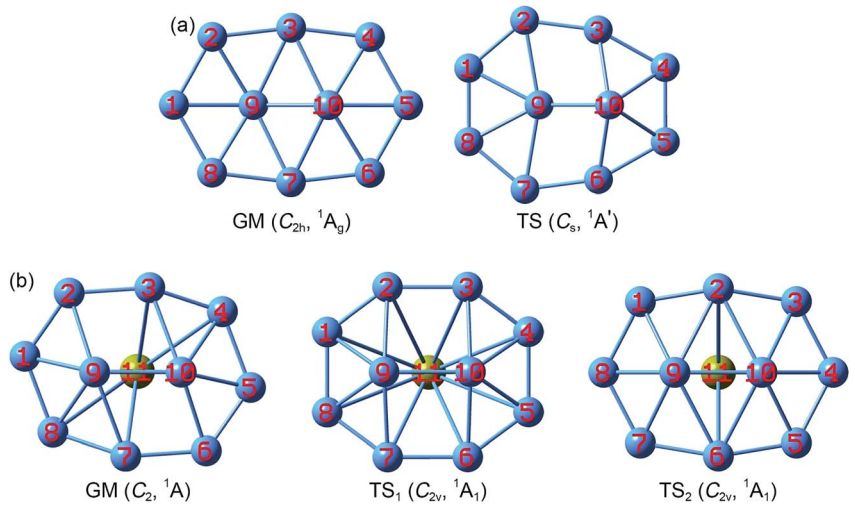

Fig. 1 Optimized structures of (a) B_{10} (C_{2h}, ^1A_g) global minimum (GM) and (b) $B_{10}Ca$ (C_2, ^1A) GM at the PBE0/6-311+G* level. Also shown are their transition-state (TS) structures associated with in-plane rotation: B_{10} TS (C_s, $^1A'$), $B_{10}Ca$ TS$_1$ (C_{2v}, $^1A_1$), and $B_{10}Ca$ TS$_2$ (C_{2v}, $^1A_1$). Two TS structures are found for $B_{10}Ca$, which effectively correspond to clockwise and anticlockwise rotations of the peripheral B_8 ring around the B_2 core, respectively. See Fig. S2 (ESI†) for their bond distances.

shrinkage at the other, and atom B10 being substantially popped out.[51] The changes hinder the interconversion between GM and TS. The anticipated barrier lies in the distinct coordination environments: two hexacoordinate B centers in GM *versus* one heptacoordinate B and one pentacoordinate B in TS.

Structural parameters of $B_{10}Ca$ and B_{10} GM/TS clusters at PBE0 are presented in Fig. S2 (ESI†). All five structures have similar perimeters for the outer B_8 ring: 12.5–12.8 Å. However, bond distances in the inner B_2 core are slightly expanded from 1.63–1.66 Å in B_{10} to 1.70–1.72 Å in $B_{10}Ca$. Radial B–B links are 1.79 Å in average for $B_{10}Ca$ GM, which are elongated relative to B_{10} GM (1.70 Å in average). Thus, upon Ca alloying, interior B–B links undergo discernible expansion, leading to bowl-like $B_{10}Ca$ clusters (GM, TS$_1$, and TS$_2$). Note that such changes do not necessarily imply that interior B–B links in $B_{10}Ca$ have lower bond orders (*vide infra*).

3.2. Wiberg bond indices and natural atomic charges

The NBO analyses provide quantitative data for WBIs (Fig. 2) and natural atomic charges (Fig. S3, ESI†). WBIs are highly non-uniform among peripheral and interior B–B links, between GM and TS structures, and between $B_{10}Ca$ and B_{10} clusters. We mention a couple of general observations. First, WBIs on the periphery are greater than 1.0, whereas those for interior links are below 1.0. The observation implies that the periphery is bound by two-center two-electron (2c–2e) skeleton σ bonds along with delocalized π/σ bonds. In contrast, interior B–B links are entirely held together by delocalized π/σ clouds. Second, there appears to be enhanced peripheral bonding in $B_{10}Ca$ GM (WBIs in total: 10.1) as compared to B_{10} GM (WBIs in total: 9.6). Third, WBIs of B–Ca links in $B_{10}Ca$ GM are minor: 0.07/0.10/0.15 for the B9–Ca/B3–Ca/B4–Ca links, suggesting negligible covalent bonding between Ca and B atoms.

Natural atomic charges in the $B_{10}Ca$ GM cluster (Fig. S3b, ESI†) are consistent with a charge transfer complex: $[B_{10}]^{2-}[Ca]^{2+}$. Specifically, Ca atom has a positive charge of +1.52 $|e|$, with the peripheral B_8 ring collectively carrying a negative charge of −1.44 $|e|$ and the inner B_2 dimer being roughly neutral. Note that atoms B4 and B8 each has −0.31 $|e|$, which are the most negative due to their closeness to the Ca center. The B_{10} GM (Fig. S3a, ESI†) shows intramolecular charge redistribution, so that the central B9B3B10B7 diamond carries negative charges (−0.22/−0.17 $|e|$ per atom) and the four B2/B4/B6/B8 corners are positive (+0.20 $|e|$ per atom). Going from B_{10} GM to $B_{10}Ca$ GM, the major change in charges also lies in the above four corners, where the B4/B8 centers each gains −0.51 $|e|$ from Ca and B2/B6 each gets −0.35 $|e|$. Overall, the distribution of negative charges is more uniform in $B_{10}Ca$ GM relative to B_{10} GM.[52]

4. Discussion

4.1. Chemical bonding in the $B_{10}Ca$ cluster

The nature of bonding ultimately governs the dynamic fluxionality of a molecular system. Therefore, we start our discussion with chemical bonding in $B_{10}Ca$ cluster. Considering the electron configurations of B $2s^22p^1$ and Ca $4s^2$, the $B_{10}Ca$ cluster has 32 valence electrons. The occupied CMOs are all based on the B_{10} fragment (Fig. 3), consistent with a $[B_{10}]^{2-}[Ca]^{2+}$ charge-transfer complex; see above. The CMOs can be straightforwardly sorted into three categories. Subset (a) is primarily clouded on the periphery with major contributions from B 2s atomic orbitals (AOs). These CMOs have 0 to 4 nodal planes from bottom up (with three quasi-degenerate pairs in the middle), which follow the orbital building principles and readily recombine as eight 2c–2e Lewis B–B σ single bonds on the periphery.[53]

For the π framework in subset (c), three CMOs have 0 and 1 (quasi-degenerate) nodal planes, where the intrinsic nodal plane associated with p_z AOs is not counted, as routine. The

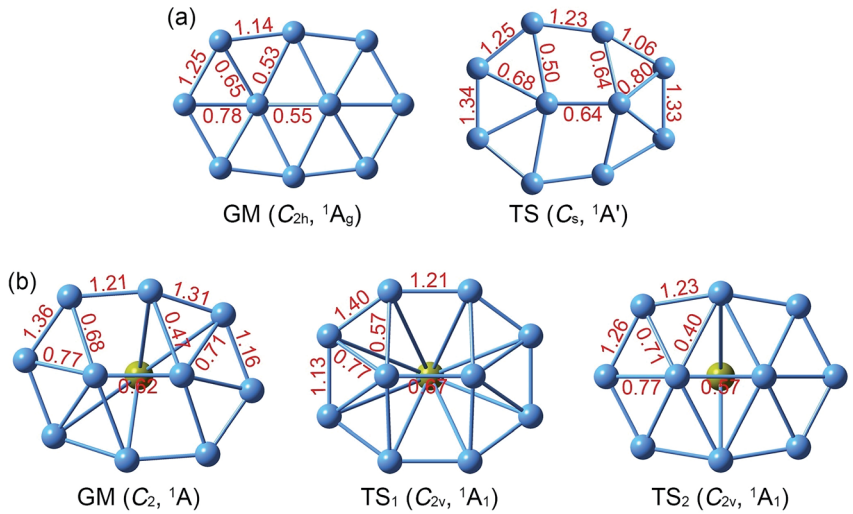

Fig. 2 Calculated Wiberg bond indices (WBIs) from natural bond orbital (NBO) analysis at the PBE0/6-311G* level. (a) B_{10} GM and TS. (b) $B_{10}Ca$ GM, TS_1, and TS_2.

three CMOs are analogous to the prototypical π sextet in benzene, thus endowing the $B_{10}Ca$ cluster with π aromaticity according to the $(4n + 2)$ Hückel rule. The Ca atom only contributes less than 7% in these π CMOs. For the delocalized σ framework (subset (b)), the five CMOs again follow the orbital building principles with 0 up to 2 nodal planes (including two quasi-degenerate pairs). This CMO pattern makes it imperative to claim σ aromaticity for the $B_{10}Ca$ cluster. Indeed, the 10σ electron-counting conforms to the $(4n + 2)$ Hückel rule. In summary, the CMO analysis indicates that the $B_{10}Ca$ cluster possesses π/σ double aromaticity with 6π and 10σ electrons, respectively. In this model, there are no 2c–2e Lewis B–B π/σ bonds inside the peripheral B_8 ring, which explains why all those B–B links have low WBI values (less than 1.0; Fig. 2b).

The bonding picture is borne out from electron localization functions (ELFs)[54] and AdNDP analysis (Fig. 4). The ELF_π and

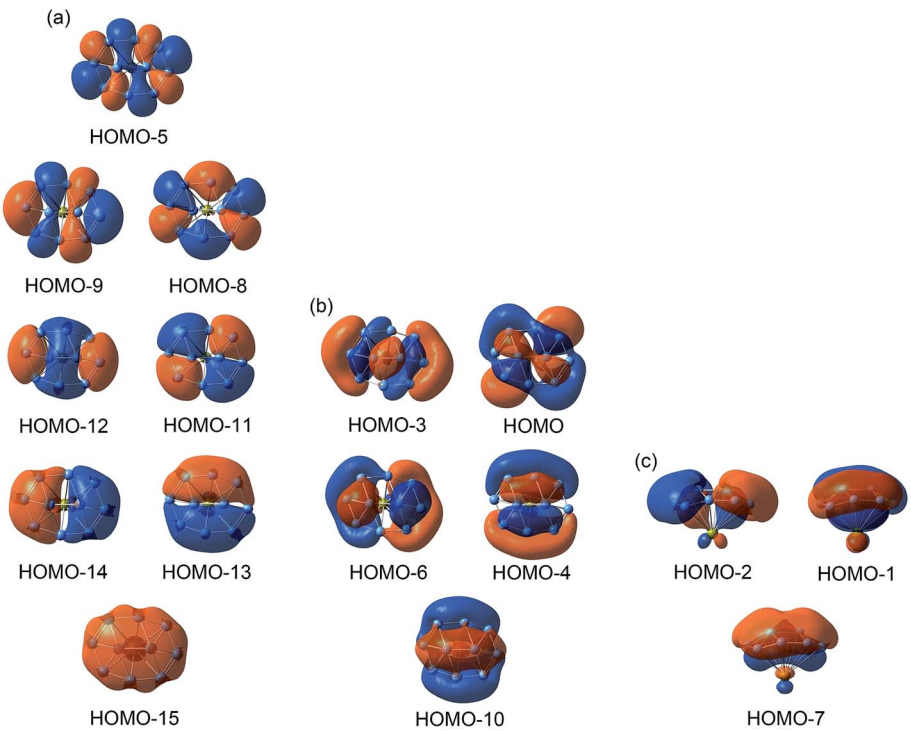

Fig. 3 Pictures of occupied canonical molecular orbitals (CMOs) of $B_{10}Ca$ GM cluster, calculated at the PBE0/6-311+G* level. The CMOs are sorted to three subsets: (a) peripheral two-center two-electron (2c–2e) Lewis B–B σ single bonds; (b) global, delocalized 10σ framework; and (c) global, delocalized 6π framework.

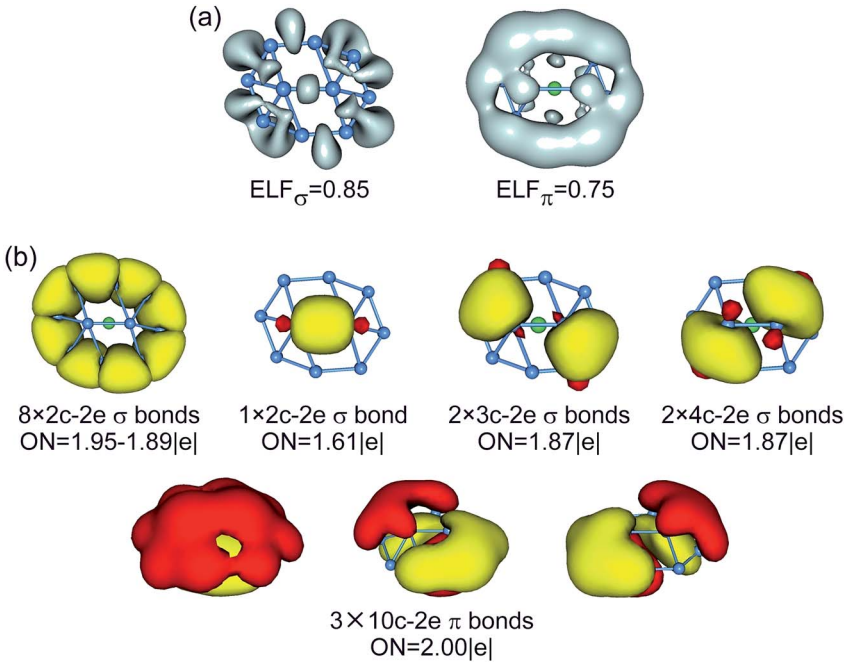

Fig. 4 (a) Electron localization functions, ELF$_\sigma$ and ELF$_\pi$, of $B_{10}Ca$ GM cluster. (b) Chemical bonding pattern of $B_{10}Ca$ GM cluster on the basis of adaptive natural density partitioning (AdNDP) analysis, wherein the global 10σ framework is approximated to "island" σ bonds. Occupation numbers (ONs) are indicated.

ELF$_\sigma$ data are consistent with localized Lewis bonds on the periphery, as well as delocalized π/σ frameworks. The AdNDP scheme of $B_{10}Ca$ cluster (Fig. 4b) reproduces peripheral 2c–2e σ bonds[53] and global π bonds. For the delocalized σ framework, we chose to partition it as one 2c–2e σ bond on the inner B_2 dimer and four 3c–2e/4c–2e σ bonds around the four corners, as hinted by the ELF$_\sigma$ data. It should be stressed that this "island" σ scheme is only an approximation. In particular, the 2c–2e σ bond has an occupation number (ON) of 1.61 $|e|$ only. Nonetheless, the scheme is useful in elucidating the structural dynamics (*vide infra*).

The CMOs, ELFs, and AdNDP schemes of TS_1/TS_2 structures of the $B_{10}Ca$ cluster are shown in Fig. 5 and S4–S6 (ESI†). The basic bonding information is similar to that described above, except for a slight spatial shift of the π/σ clouds, which is associated with geometric changes between GM and TS_1/TS_2 structures. For example, the AdNDP scheme for the 10σ framework in TS_1 (Fig. 5b) is similar to that in the GM (Fig. 4b). However, upon clockwise rotation of TS_1 relative to GM, two diamond 4c–2e σ bonds in the GM shrink spatially and become 3c–2e ones. This effectively generates a flow of σ clouds within the islands, whose direction is anticlockwise. For a following step (not shown), certain 3c–2e σ bonds may expand to 4c–2e ones. Therefore, during dynamic rotation of the $B_{10}Ca$ cluster, delocalized σ clouds flow (and shrink/expand) continuously like a liquid and counter the direction of geometric rotation, which are maintained approximately on the four corner islands and underlie the low rotation barrier. The delocalized π clouds behave similarly.

For comparison, the CMOs, ELFs, and AdNDP patterns of GM/TS structures of bare B_{10} cluster are shown in Fig. 6 and S7–S9 (ESI†). The B_{10} GM cluster (Fig. S7b, ESI†) differs from $B_{10}Ca$ GM (Fig. 3b) by one CMO less in the delocalized σ framework, which becomes the lowest unoccupied molecular orbital (LUMO) in the former species. Based on the above understanding of $B_{10}Ca$, bare B_{10} cluster should be classified as σ antiaromatic, which has a delocalized 8σ system and follows the 4*n* Hückel rule.[55,56] Indeed, the B_{10} cluster is more elongated than $B_{10}Ca$, a typical consequence of σ antiaromaticity; see Section 3.1.[50] Overall, the B_{10} cluster has conflicting aromaticity with 6π and 8σ electrons.

It is interesting to quantitatively follow the orbital contributions of the inner B_2 core in $B_{10}Ca$ GM and B_{10} GM clusters. The B_2 core in $B_{10}Ca$ contributes 3.32, 1.84, and 0.87 $|e|$ to subsets (a)–(c), respectively (Fig. 3), compared to 3.89, 1.02, and 1.52 $|e|$ in B_{10} (Fig. S7, ESI†). In other words, the B_2 core has similar total contributions to σ CMOs: 5.16 $|e|$ in $B_{10}Ca$ *versus* 4.91 $|e|$ in B_{10}. However, its contributions to π CMOs differ for the species: 0.87 $|e|$ in $B_{10}Ca$ *versus* 1.52 $|e|$ in B_{10}. The latter observation suggests that the π clouds are probably more delocalized on the plane in B_{10} GM, which is a con for the dynamic fluxionality of bare B_{10} cluster, in particular considering that it has a rugged shape. In contrast, the π clouds in $B_{10}Ca$ GM appear to lean to the periphery, which benefits a low dynamic barrier, as supported by the comparative ELF$_\pi$ patterns (Fig. 4a *versus* Fig. 6a). The above data also indicate that the B_2 core has collectively 5.84 $|e|$ in $B_{10}Ca$ GM *versus* 6.43 $|e|$ in B_{10} GM. Indeed, NBO data on natural atomic charges show that the B_2 core is practically neutral in $B_{10}Ca$ and negatively charged in B_{10} (by −0.22 $|e|$ per atom; Fig. S3, ESI†).

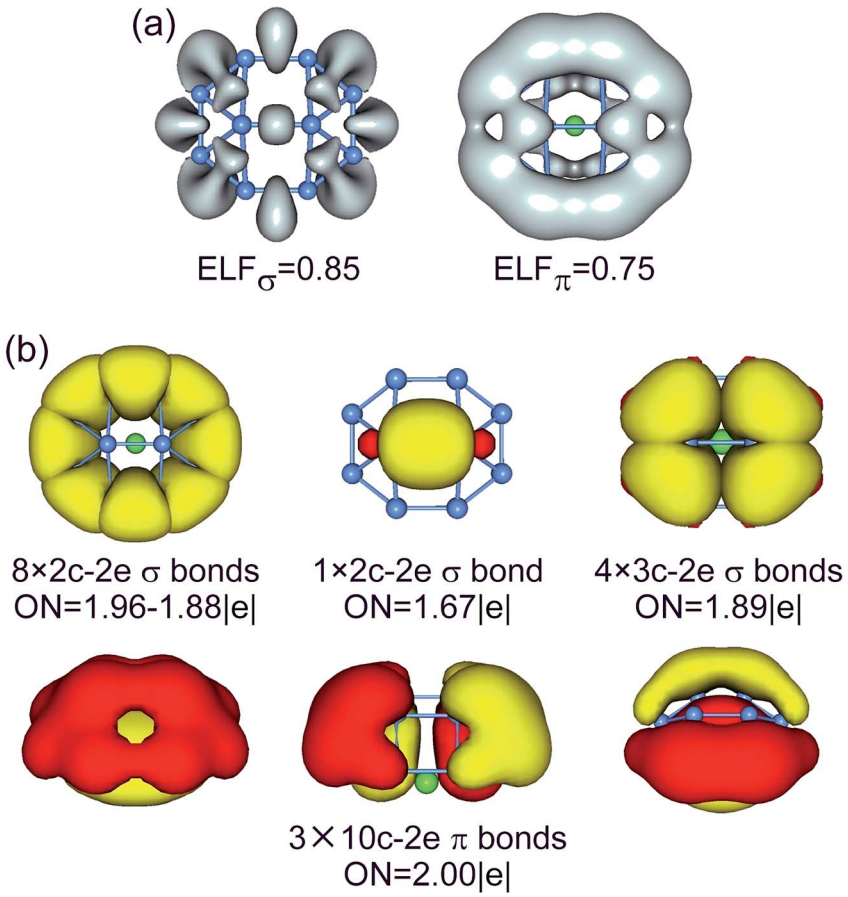

Fig. 5 (a) ELF$_\sigma$ and ELF$_\pi$ of $B_{10}Ca$ TS_1 cluster. (b) AdNDP bonding pattern of $B_{10}Ca$ TS_1 cluster, wherein the global 10σ framework is approximated to island σ bonds. ONs are indicated.

4.2. Starting a subnanoscale tank tread: distinct structural dynamics of $B_{10}Ca$ and B_{10} clusters

Two key structural features of the present $B_{10}Ca$ and B_{10} systems make it rather challenging to tune/control their rotation barriers. First, the clusters assume elongated (rather than circular) geometries akin to tank treads, which are generally less fluxional than molecular Wankel motors. Second, bare B_{10} cluster is composed entirely of close-packed B_3 triangles without "defect" holes, which is intuitively anticipated to be rigid against deformation. Nonetheless, the energetics data in Section 3.1 clearly show that Ca alloying in the $B_{10}Ca$ GM cluster effectively diminishes its rotation barrier down to 0.95 and 1.25 kcal mol^{-1} at the PBE0 level, with respect to TS_1 and TS_2, respectively. This is a remarkable achievement considering that bare B_{10} cluster is nonfluxional with a barrier of 12.32 kcal mol^{-1}. To our knowledge, this is the first example of barrier reduction of a molecular rotor by one order of magnitude and down to ~1 kcal mol^{-1},[17,18] a highly desirable level for dynamic fluxionality.

With the GM and TS_1/TS_2 structures of the $B_{10}Ca$ cluster being identified (Fig. 1b), the dynamic structural evolution is relatively simple as illustrated in Fig. 7, assuming that the peripheral ring rotates clockwise. Starting with GM_1 and let the B9–B2 link rotate by about 18.9°, one reaches TS_{1-2} that corresponds to TS_1 in Fig. 1b. From GM_1 to TS_{1-2}, rhombic B2B3B10B9 and B7B9B10B6 holes turn to squares. Going down the barrier, the B9–B2 link rotates by another 17.5° and the system returns to GM_2. Due to the chiral nature of $B_{10}Ca$ cluster with C_2 symmetry, GM_1 and GM_2 are a pair of enantiomers and thus isoenergetic. However, the system does not recover its initial orientation. Further rotating the B9–B2 link slightly by 7.1° and making the B10–B2 and B9–B6 links, one reaches TS_{2-3}. The latter differs from TS_{1-2} with a higher barrier and it corresponds to TS_2 in Fig. 1b. From TS_{2-3} to GM_3, the B9–B2 link rotates another 7.1° and breaks, generating two new rhombic holes: B1B2B10B9 and B6B9B10B5. This completes a fully cycle, in which the cluster returns to its initial structure as well as orientation. During this process, the peripheral ring moves by one B–B link (or about 51°).

Despite being nonfluxional with a substantial barrier, the structural evolution of bare B_{10} cluster can be followed on the basis of GM and TS structures identified. The process is simpler (Fig. 8). Upon rotation of the B9–B2 link clockwise by 12.0°, the B9–B3 link breaks and two rhombic B9B2B3B10 and B7B9B10B6 holes emerge, which leads to TS_{1-2} that corresponds to TS in Fig. 1a. Further rotate the B9–B2 link by 38.1° and the system recovers GM_2. Overall, the peripheral atoms move by one B–B link (or about 50°) from GM_1 to GM_2.

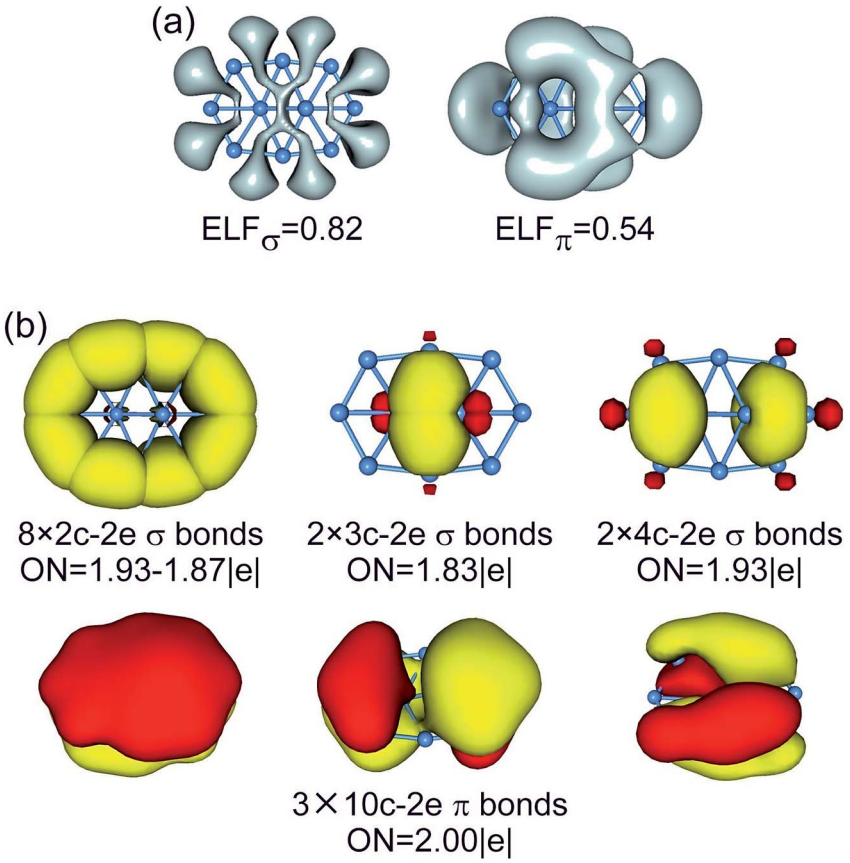

Fig. 6 (a) ELF$_\sigma$ and ELF$_\pi$ of B_{10} GM cluster. (b) AdNDP bonding pattern of B_{10} GM cluster, wherein the global 8σ framework is approximated to island σ bonds. ONs are indicated.

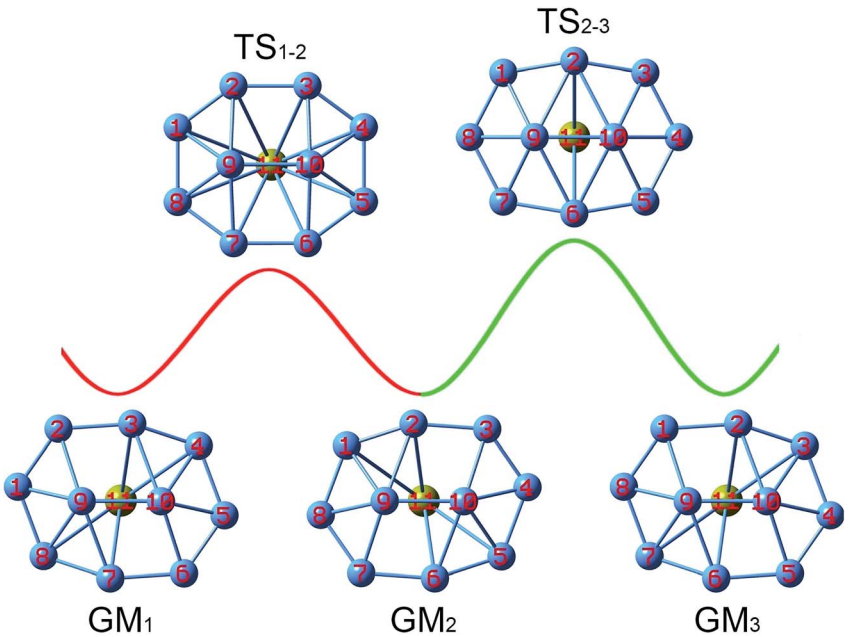

Fig. 7 Structural evolution of the $B_{10}Ca$ GM cluster during dynamic rotation, assuming that the peripheral B_8 ring moves clockwise around the B_2 core. Two energy barriers, TS_{1-2} and TS_{2-3}, are to be overcome for the cluster in order to fully recover its initial structure and orientation. These barriers correspond to the TS_1 and TS_2 structures (Fig. 1b), respectively.

To demonstrate the dynamic fluxionality of $B_{10}Ca$ cluster, we performed BOMD simulations at selected temperatures of 300, 600, and 900 K. A typical simulation at 900 K is presented in the form of a short movie (see the ESI†), which was carried out for 50 ps using the CP2K package at the PBE0/DZVP level. Initial conditions were chosen to correspond to the microcanonical ensemble (NVE). The extracted movie roughly covers a time span of 2.5 ps. It is obvious that at 900 K the $B_{10}Ca$ cluster behaves vividly like a subnanoscale tank tread, with the peripheral B_8 ring gliding freely as a flexible chain around the B_2 core. In particular, the peripheral B_8 ring appears to be rather robust during rotation, which rotates but does not break. Similar motion is observed at 600 K except that it is slower, whereas preliminary data at 300 K do not reveal dynamic fluxionality.

As for mechanisms that distinguish between the dynamic properties of $B_{10}Ca$ and B_{10} clusters, the most important one is their bonding, as detailed in Section 4.1. Note that in prior studies people have attempted to unravel the connection between aromaticity (or electron delocalization) and fluxionality, in which the magnetic response is discussed.[57] The present data offer key insights using the CMOs and AdNDP analyses. While both $B_{10}Ca$ and B_{10} are 6π aromatic, they differ in the σ framework: B_{10} is σ antiaromatic[55,56] with 8σ electrons and $B_{10}Ca$ has σ aromaticity (10σ electrons). Double π/σ aromaticity in $B_{10}Ca$ cluster makes it sort of circular with a smooth bowl-shaped surface, facilitating π/σ delocalization and structural fluxionality. In contrast, the B_{10} cluster has a rugged surface[51] and deteriorated π/σ delocalization.

In terms of geometry, the C_2 symmetry of $B_{10}Ca$ GM cluster (Fig. 1b) has two rhombic defect holes, while B_{10} GM cluster features triangular close-packing. Such defects are known to be critical for the dynamic fluxionality of subnanoscale tank treads (and nanorotors in general).[10] Thus, alloying with Ca induces structural flexibility for $B_{10}Ca$ cluster, which serves as "pre-activation" of the system and effectively reduces the dynamic barrier. As for the B_{10} cluster, 8σ antiaromaticity leads to an elongated GM as well as substantial geometric changes between GM and TS (Fig. 1a): expansion at the left side *versus* shrinkage at the right. In fact, while delocalized σ clouds in the GM are balanced for left *versus* right (Fig. 6b), they become highly uneven in the TS so that the left side only has one 5c–2e σ bond and the right has three 3c–2e/4c–2e bonds (Fig. S9b, ESI†). Such a change is induced entirely by a rotation of the peripheral ring, which is an intriguing consequence of σ antiaromaticity and clearly underlies its large barrier. Lastly, we comment on a consequence of the two inequivalent TS structures of $B_{10}Ca$ cluster (Fig. 1b). All molecular rotors to date move randomly (clockwise or anticlockwise). However, the occurrence of two inequivalent TS structures for $B_{10}Ca$ hints that the system can at least be initiated with one direction preferred to another, which simplifies further control or manipulation of the dynamics.

4.3. Change in WBIs as a semi-quantitative indicator of dynamic fluxionality

To shed further light on the distinct dynamics of $B_{10}Ca$ and B_{10} clusters, we make use of the WBI data from NBO analyses.

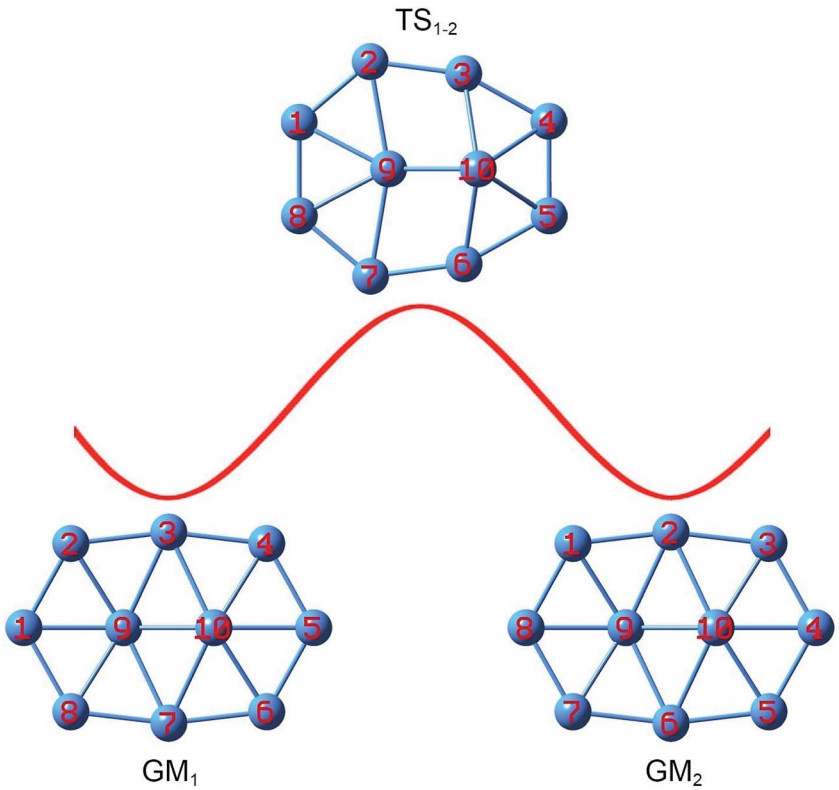

Fig. 8 Structural evolution of the B_{10} GM cluster during dynamic rotation, assuming that the peripheral B_8 ring moves clockwise around the B_2 core. Energy barrier TS_{1-2} is associated with the TS structure (Fig. 1a).

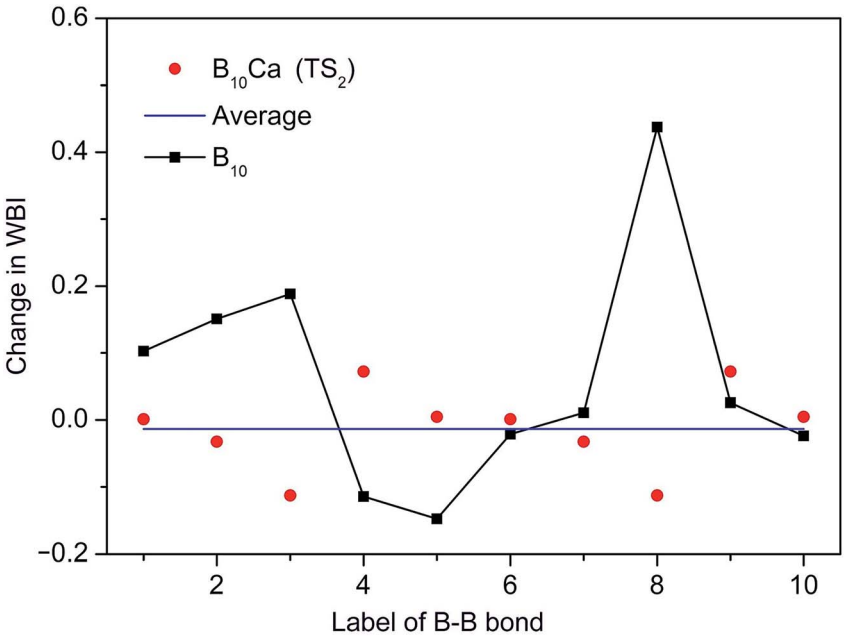

Fig. 9 Change in WBIs (that is, ΔWBIs) for the radial B–B links in the $B_{10}Ca$ cluster from GM to TS_2 during dynamic rotation. The WBI data are obtained explicitly from GM_3 to TS_{2-3} in Fig. 7 (anticlockwise rotation). The B–B links are labelled numerically, starting from the far-left link (B9–B8) as "1" and counting clockwise up to "10" (links B9–B2 and B10–B6 included). Positive ΔWBI indicates elongation and negative compression. Red dots are ΔWBIs of the $B_{10}Ca$ cluster and a horizontal blue line is their average. Comparative data of the B_{10} cluster are shown with filled squares.

Intuitively, the barrier of a molecular rotor is connected to the WBI change between the GM and TS structures, which is denoted here as ΔWBI. In the present systems, the radial links govern in-plane rotation and determine the barrier. Thus, we follow all radial B–B links. As an example, ΔWBI values of the $B_{10}Ca$ cluster with respect to TS_2 are plotted in Fig. 9, which are compared to those of bare B_{10} cluster. Here the B–B links are labeled numerically based on GM_3 and TS_{2-3} (anticlockwise rotation; Fig. 7). Link B9–B8 at the far left is labeled "1", counting clockwise up to "10". These include B9–B2 and B10–B6 as "3" and "8", respectively. By definition, a positive ΔWBI is associated with bond elongation, and *vice versa*.

The $B_{10}Ca$ cluster shows a smooth ΔWBI curve with relatively minor and uniform values for all radial B–B links, consistent with a low barrier. In contrast, large ΔWBIs and in particular spikes are present for the B_{10} cluster, whose B–B links are labeled again with the far-left one (B9–B1) being "1" and counted clockwise up to "10". Specifically, link "8" (B10–B7; Fig. 1a) has the largest ΔWBI, which has to elongate substantially and eventually break in order for the cluster to reach the TS structure, thus defining the barrier height of B_{10} cluster. For comparison, links B9–B3 and B10–B7 in $B_{10}Ca$ GM_1 (Fig. 7) are "preactivated" upon alloying with Ca atom, and they are no longer the bottleneck for fluxionality, which effectively diminish the barrier (for TS_1). Moreover, there is no need to break any B–B links from GM_3 to TS_{2-3} (anticlockwise; Fig. 7), but to shrink links B9–B2 and B10–B6, which have the largest negative ΔWBIs, in line with a low barrier for TS_2. The comparative ΔWBI data of $B_{10}Ca$ and B_{10} clusters distinguish between the two species, demonstrating a semi-quantitative measure for dynamic fluxionality.

5. Conclusions

We have demonstrated, *via* alloying with Ca atom, a means to tune the structural dynamics of a subnanoscale tank tread $B_{10}Ca$ cluster. The strategy efficiently reduces the rotation barrier by one order of magnitude, from 12 kcal mol^{-1} in B_{10} down to around 1 kcal mol^{-1} in $B_{10}Ca$. The $B_{10}Ca$ global-minimum cluster is half-sandwich in shape, which is dynamically fluxional at 600 K and beyond, whereas bare B_{10} cluster is nonfluxional. In terms of structures, Ca alloying generates two rhombic defect holes in $B_{10}Ca$ cluster, which preactivates the system for fluxionality. Chemical bonding analyses show that the $B_{10}Ca$ cluster is a charge-transfer complex and can be formulated as $[B_{10}]^{2-}[Ca]^{2+}$, featuring double (6π and 10σ) aromaticity. The bonding pattern leads to a more circular geometry and ideal π/σ delocalization, facilitating dynamic fluxionality. In contrast, the B_{10} cluster has conflicting aromaticity (6π *versus* 8σ), as well as a more elongated and rugged shape. Thus, our work demonstrates that π/σ aromaticity can be utilized as a key concept to design dynamically fluxional nanosystems. To semi-quantitatively describe dynamic fluxionality, the change in Wiberg bond indices between global-minimum and transition-state structures serves as a useful indicator, which clearly distinguishes between a fluxional $B_{10}Ca$ cluster and a nonfluxional B_{10} cluster.

Conflicts of interest

There are no conflicts to declare.

Acknowledgements

This work was supported by the National Natural Science Foundation of China (21873058, 21573138), the Natural Science Foundation of Xinzhou Teachers University (201711), and the Sanjin Scholar Distinguished Professors Program.

References

1 J. O. C. Jiménez-Halla, R. Islas, T. Heine and G. Merino, *Angew. Chem., Int. Ed.*, 2010, **49**, 5668.
2 S. Erhardt, G. Frenking, Z. F. Chen and P. v. R. Schleyer, *Angew. Chem., Int. Ed.*, 2005, **44**, 1078.
3 G. Martínez-Guajardo, A. P. Sergeeva, A. I. Boldyrev, T. Heine, J. M. Ugalde and G. Merino, *Chem. Commun.*, 2011, **47**, 6242.
4 J. Zhang, A. P. Sergeeva, M. Sparta and A. N. Alexandrova, *Angew. Chem., Int. Ed.*, 2012, **51**, 8512.
5 G. Merino and T. Heine, *Angew. Chem., Int. Ed.*, 2012, **51**, 10226.
6 D. Moreno, S. Pan, L. L. Zeonjuk, R. Islas, E. Osorio, G. Martínez-Guajardo, P. K. Chattaraj, T. Heine and G. Merino, *Chem. Commun.*, 2014, **50**, 8140.
7 F. Cervantes-Navarro, G. Martínez-Guajardo, E. Osorio, D. Moreno, W. Tiznado, R. Islas, K. J. Donald and G. Merino, *Chem. Commun.*, 2014, **50**, 10680.
8 S. Jalife, L. Liu, S. Pan, J. L. Cabellos, E. Osorio, C. Lu, T. Heine, K. J. Donald and G. Merino, *Nanoscale*, 2016, **8**, 17639.
9 M. R. Fagiani, X. W. Song, P. Petkov, S. Debnath, S. Gewinner, W. Schöllkopf, T. Heine, A. Fielicke and K. R. Asmis, *Angew. Chem., Int. Ed.*, 2017, **56**, 501.
10 Y. J. Wang, X. Y. Zhao, Q. Chen, H. J. Zhai and S. D. Li, *Nanoscale*, 2015, **7**, 16054.
11 Y. J. Wang, X. R. You, Q. Chen, L. Y. Feng, K. Wang, T. Ou, X. Y. Zhao, H. J. Zhai and S. D. Li, *Phys. Chem. Chem. Phys.*, 2016, **18**, 15774.
12 Y. J. Wang, J. C. Guo and H. J. Zhai, *Nanoscale*, 2017, **9**, 9310.
13 Y. G. Yang, D. M. Jia, Y. J. Wang, H. J. Zhai, Y. Man and S. D. Li, *Nanoscale*, 2017, **9**, 1443.
14 Y. J. Wang, L. Y. Feng, J. C. Guo and H. J. Zhai, *Chem.–Asian J.*, 2017, **12**, 2899.
15 J. C. Guo, L. Y. Feng, Y. J. Wang, S. Jalife, A. Vásquez-Espinal, J. L. Cabellos, S. Pan, G. Merino and H. J. Zhai, *Angew. Chem., Int. Ed.*, 2017, **56**, 10174.
16 L. Y. Feng, J. C. Guo, P. F. Li and H. J. Zhai, *Phys. Chem. Chem. Phys.*, 2018, **20**, 22719.
17 I. A. Popov, W. L. Li, Z. A. Piazza, A. I. Boldyrev and L. S. Wang, *J. Phys. Chem. A*, 2014, **118**, 8098.
18 L. Liu, D. Moreno, E. Osorio, A. C. Castro, S. Pan, P. K. Chattaraj, T. Heine and G. Merino, *RSC Adv.*, 2016, **6**, 27177.
19 W. Huang, A. P. Sergeeva, H. J. Zhai, B. B. Averkiev, L. S. Wang and A. I. Boldyrev, *Nat. Chem.*, 2010, **2**, 202.
20 E. Oger, N. R. M. Crawford, R. Kelting, P. Weis, M. M. Kappes and R. Ahlrichs, *Angew. Chem., Int. Ed.*, 2007, **46**, 8503.
21 L. Hanley, J. L. Whitten and S. L. Anderson, *J. Phys. Chem.*, 1988, **92**, 5803.
22 J. E. Fowler and J. M. Ugalde, *J. Phys. Chem. A*, 2000, **104**, 397.
23 J. Aihara, *J. Phys. Chem. A*, 2001, **105**, 5486.
24 J. Aihara, H. Kanno and T. Ishida, *J. Am. Chem. Soc.*, 2005, **127**, 13324.
25 H. J. Zhai, A. N. Alexandrova, K. A. Birch, A. I. Boldyrev and L. S. Wang, *Angew. Chem., Int. Ed.*, 2003, **42**, 6004.
26 H. J. Zhai, B. Kiran, J. Li and L. S. Wang, *Nat. Mater.*, 2003, **2**, 827.
27 B. Kiran, S. Bulusu, H. J. Zhai, S. Yoo, X. C. Zeng and L. S. Wang, *Proc. Natl. Acad. Sci. U. S. A.*, 2005, **102**, 961.
28 A. P. Sergeeva, D. Y. Zubarev, H. J. Zhai, A. I. Boldyrev and L. S. Wang, *J. Am. Chem. Soc.*, 2008, **130**, 7244.
29 Z. A. Piazza, H. S. Hu, W. L. Li, Y. F. Zhao, J. Li and L. S. Wang, *Nat. Commun.*, 2014, **5**, 3113.
30 H. J. Zhai, Y. F. Zhao, W. L. Li, Q. Chen, H. Bai, H. S. Hu, Z. A. Piazza, W. J. Tian, H. G. Lu, Y. B. Wu, Y. W. Mu, G. F. Wei, Z. P. Liu, J. Li, S. D. Li and L. S. Wang, *Nat. Chem.*, 2014, **6**, 727.
31 W. L. Li, Q. Chen, W. J. Tian, H. Bai, Y. F. Zhao, H. S. Hu, J. Li, H. J. Zhai, S. D. Li and L. S. Wang, *J. Am. Chem. Soc.*, 2014, **136**, 12257.
32 Q. Chen, W. L. Li, Y. F. Zhao, S. Y. Zhang, H. S. Hu, H. Bai, H. R. Li, W. J. Tian, H. G. Lu, H. J. Zhai, S. D. Li, J. Li and L. S. Wang, *ACS Nano*, 2015, **9**, 754.
33 Y. J. Wang, Y. F. Zhao, W. L. Li, T. Jian, Q. Chen, X. R. You, T. Ou, X. Y. Zhao, H. J. Zhai, S. D. Li, J. Li and L. S. Wang, *J. Chem. Phys.*, 2016, **144**, 064307.
34 Q. Chen, W. J. Tian, L. Y. Feng, H. G. Lu, Y. W. Mu, H. J. Zhai, S. D. Li and L. S. Wang, *Nanoscale*, 2017, **9**, 4550.
35 A. N. Alexandrova, A. I. Boldyrev, H. J. Zhai and L. S. Wang, *Coord. Chem. Rev.*, 2006, **250**, 2811.
36 A. P. Sergeeva, I. A. Popov, Z. A. Piazza, W. L. Li, C. Romanescu, L. S. Wang and A. I. Boldyrev, *Acc. Chem. Res.*, 2014, **47**, 1349.
37 Borospherene B_{40} cluster is shown to behave dynamically like a nanobubble at high temperatures. See: G. Martínez-Guajardo, J. L. Cabellos, A. Díaz-Celaya, S. Pan, R. Islas, P. K. Chattaraj, T. Heine and G. Merino, *Sci. Rep.*, 2015, **5**, 11287.
38 M. Saunders, *J. Comput. Chem.*, 2004, **25**, 621.
39 P. P. Bera, K. W. Sattelmeyer, M. Saunders, H. F. Schaefer III and P. v. R. Schleyer, *J. Phys. Chem. A*, 2006, **110**, 4287.
40 R. Krishnan, J. S. Binkley, R. Seeger and J. A. Pople, *J. Chem. Phys.*, 1980, **72**, 650.
41 C. Adamo and V. Barone, *J. Chem. Phys.*, 1999, **110**, 6158.
42 J. A. Pople, M. Head-Gordon and K. Raghavachari, *J. Chem. Phys.*, 1987, **87**, 5968.
43 G. E. Scuseria, C. L. Janssen and H. F. Schaefer III, *J. Chem. Phys.*, 1988, **89**, 7382.
44 G. E. Scuseria and H. F. Schaefer III, *J. Chem. Phys.*, 1989, **90**, 3700.
45 A. E. Reed, L. A. Curtiss and F. Weinhold, *Chem. Rev.*, 1988, **88**, 899.
46 D. Y. Zubarev and A. I. Boldyrev, *Phys. Chem. Chem. Phys.*, 2008, **10**, 5207.
47 J. VandeVondele, M. Krack, F. Mohamed, M. Parrinello, T. Chassaing and J. Hutter, *Comput. Phys. Commun.*, 2005, **167**, 103.

48 M. J. Frisch, *et al.*, *Gaussian 09, revision D.01*, Gaussian Inc., Wallingford, Connecticut, 2009.
49 U. Varetto, *Molekel 5.4.0.8*, Swiss National Supercomputing Center, Manno, Switzerland, 2009.
50 The B_{10} GM cluster has a length of 4.76 Å and width of 3.13 Å (with length-to-width ratio of 1.52). Those of the B_{10} TS, $B_{10}Ca$ TS_1, and $B_{10}Ca$ TS_2 species are 4.13/3.54, 4.01/3.38, and 4.50/3.28 Å, with ratios of 1.17, 1.19, and 1.37, respectively. Thus, there is a marked ratio change from B_{10} GM to B_{10} TS. Also, $B_{10}Ca$ TS_1 is particularly circular.
51 Of all five key structures in Fig. 1, the peripheral B_8 ring is perfectly planar only in B_{10} GM. For other species, the out-of-plane distortions of central B atoms are estimated roughly. In B_{10} GM cluster, atom B9 is slightly out-of-plane toward inside (by 0.3 Å) and B10 toward the opposite side. For the B_{10} TS, $B_{10}Ca$ TS_1, and $B_{10}Ca$ TS_2 species, atoms B9/B10 are popped out by 0.3/1.0, 0.9/0.9, and 0.8/0.8 Å, respectively.
52 There appears to be a general trend that a B center with a higher coordination and stronger bonds gets some net negative charges from surrounding B atoms. In this way, the hexacoordinate B9/B10 centers and tetracoordinate B3/B7 atoms in B_{10} GM carry negative charges (Fig. S3a; ESI†). For B_{10} TS, the B10 center remains strongly coordinated by five B atoms, whereas the B9 center is only loosely bound despite its heptacoordination nature. The latter leads to less negative charge.
53 Strictly speaking, the assignment of eight peripheral Lewis σ bonds is an approximation. The bottom five of these CMOs have nonnegligible contributions from central B9/B10 atoms (Fig. 3a). Quantitatively, the B9/B10 core accounts for 20.7% of these eight σ CMOs, which explains why their occupation numbers (ONs; Fig. 4b) in the AdNDP scheme deviate from an ideal value of 2.00 $|e|$.
54 B. Silvi and A. Savin, *Nature*, 1994, **371**, 683.
55 A previous work[56] assigned the delocalized σ framework of B_{10} GM cluster as one 2c–2e σ bond in B_2 core (although specifically called for caution) and three global σ bonds. The latter were proposed to render σ aromaticity for B_{10} cluster, due to the 6σ electron-counting. Our present analysis suggests that all these 8σ electrons should be treated collectively (Fig. S7b, ESI†) and B_{10} cluster is σ antiaromatic rather than σ aromatic. Indeed, the ELF_σ data and our AdNDP scheme (island version; Fig. 6) do not support the idea of a 2c–2e σ bond within the B_2 core.
56 D. Y. Zubarev and A. I. Boldyrev, *J. Comput. Chem.*, 2007, **28**, 251.
57 R. Islas, T. Heine and G. Merino, *Acc. Chem. Res.*, 2012, **45**, 215.